Volume 1 | Number 1 | Jan 2013 | Pages 1–100

Journal of
Materials Chemistry C

Materials for optical and electronic devices
www.rsc.org/materialsC

ROYAL SOCIETY
OF CHEMISTRY

ROYAL SOCIETY
OF CHEMISTRY

www.rsc.org/materialsC

Journal of Materials Chemistry C

ARTICLE

Mode coupling between nonpolar and polar phonons as the origin of improper ferroelectricity in hexagonal LuMnO₃

Seungwoo Song,[a] Jung-Hoon Lee,[a] and Hyun Myung Jang[*ab] ,

Currently, the most puzzling problem associated with the hexagonal LuMnO₃ (h-LMO) is a large temperature-gap between the structural phase transition to the polar $P6_3cm$ phase at ~1290 K and the emergence of the spontaneous polarization at a substantially reduced temperature, ~750 K. Interestingly, this large temperature-gap is not limited to h-LMO but is a universal phenomenon valid for other rare-earth manganites. We have examined this important issue by exploiting first-principles calculations. It is shown that the structural phase transition to the polar $P6_3cm$ phase from the nonpolar $P6_3/mmc$ phase of h-LMO is mediated by the freezing-in of the zone-boundary K_3 phonon. However, the ferroelectric polarization remains at a negligibly small value until the amplitude of K_3 phonon becomes a certain critical value above which the coupling of the polar Γ_2^- mode with the nonpolar K_3 mode is practically turned on. This coupling-induced polarization explains the observed temperature-gap in h-LMO as well as other rare-earth manganites.

1. Introduction

Multiferroic materials exhibit simultaneous ferroic responses with cross-coupled electric, magnetic, and structural orders.[1] Over the past decade, there has been a resurgence of interest in understanding and technological applications of multiferroics.[1-7] Multiferroics have received a great deal of attention owing to their potential for enabling new device paradigms that are based on the cross-coupling between distinct order parameters.[3-7] Among numerous multiferroic materials, manganite-based oxides have been most extensively studied. Orthorhombic manganites such as TbMnO₃ and TbMn₂O₅ exhibit a strong tendency of the magnetoelectric (ME) coupling which stems from noncollinear spin-ordering-induced improper or pseudo-proper ferroelectricity.[7,8] In hexagonal manganites (h-RMnO₃), on the other hand, asymmetric movement of rare-earth (R) cations from the centrosymmetric position is known to be a prevailing factor in the manifestation of ferroelectricity .[9-11]

Since the thermodynamic stability of h-RMnO₃ enhances with decreasing radius of R cation,[12,13] LuMnO₃ is expected to show the highest stability towards the hexagonal phase among 15 different lanthanide-based manganites. Currently, the most puzzling problem associated with the hexagonal LuMnO₃ (h-LMO) is the observed large temperature-gap between the structural phase transition to the polar $P6_3cm$ phase at ~1290 K[14,15] and the emergence of the spontaneous polarization (P_s) at

a substantially reduced temperature of ~750 K.[16] It was reported that the appearance of $\mathbf{P_s}$ is accompanied with the enhanced electron density between Lu and axial oxygen ions.[17] Interestingly, this large temperature-gap (ΔT_h) is not limited to h-LMO but is a universal phenomenon valid for other rare-earth manganites. According to the previous report,[18] ΔT_h is in the rage of 250 and 540 K with the largest gap occurring in h-LMO: ΔT_h for h-YMnO₃, h-ErMnO₃, h-YbMnO₃, and h-LuMnO₃ (h-LMO) are 300 K, 477 K, 277 K, and 540 K, respectively.[18] Thus, it is of great scientific importance to elucidate the origin of this universal phenomenon.

In the present study, to resolve this puzzling issue, we have examined the ferroelectricity origin of h-LMO by analyzing the phonon-amplitude-dependent Kohn-Sham (K-S) energy. On the basis of *ab initio* density-functional theory (DFT) calculations, we have shown that the structural phase transition to the polar $P6_3cm$ phase from the nonpolar $P6_3/mmc$ phase is mediated by the freezing-in of the zone-boundary K_3 phonon. However, the spontaneous ferroelectric polarization remains at a negligibly small value until the amplitude of K_3 phonon becomes a certain critical value above which the coupling of the polar Γ_2^- mode with the nonpolar K_3 mode is practically turned on.

2. Computational details

We have performed DFT calculations on the basis of the generalized gradient approximation (GGA)[19] and GGA+U method[20] implemented with projector augmented wave pseudopotential[21] using the *Vienna ab initio Simulation Package*.[22] All the DFT calculations were performed by adopting (i) a 5×5×3 Monkhorst-Pack k-point mesh[23] centered at Γ, (ii) a 500-eV plane-wave cutoff energy, and (iii) the tetrahedron method with Blöchl corrections for the Brillouin-zone integrations.[24] We explicitly treated nine valence electrons for Lu($5p^6 5d^1 6s^2$), seven for Mn($3d^5 4s^2$), and six for O($2s^2 2p^4$). Lu $4f$ electrons were treated as a frozen core. The structural optimizations were performed for the 30-atom-cell which corresponds to a hexagonal unit cell consisting of six formula units. The ions were relaxed until the Hellmann-Feynmann forces on them were less than 0.01 eV/Å. The Hubbard U_{eff} of 8.0 eV for the Mn $3d$-orbital was chosen on the basis of the previous work on the on-site Coulomb (U_{eff}) and intra-atomic exchange (J) parameters for h-YMnO$_3$.[25] The ferroelectric polarization was evaluated by applying the Berry-phase method.[25] Atomic displacement eigenvectors for normal modes relevant to the $P6_3/mmc$-to-$P6_3cm$ phase transition were evaluated by using the Bilbao Crystallographic Server for mode-adapted analysis.[27,28]

3. Results and discussion

Crystal and spin structures

We obtained the refined crystal structures of $P6_3/mmc$ and $P6_3cm$ phases of h-LMO using the conjugated gradient algorithm for iterative calculations.[29] The optimized lattice parameters for each phase were obtained by calculating the K-S energy as a function of the unit-cell volume and finding its minimum which corresponds to the K-S energy in the absence of external pressure. The optimized parameters are: a = 6.1441 Å, c = 11.5143 Å for $P6_3cm$ and a = 6.1400 Å, c = 11.4859 Å for $P6_3/mmc$ with the difference in the equilibrium K-S energy of 1.06 eV per unit cell. As shown in Fig. 1(a), both types of hexagonal structures consist of the stacking of two layers: one layer of corner-linked MnO$_5$ bipyramids and the other layer of Lu^{3+} ions. In contrast to the paraelectric $P6_3/mmc$ cell, however, the ferroelectric $P6_3cm$ unit cell of h-RMnO$_3$ is characterized by the existence of three distinct RO$_8$ off-centering units having trigonal D_{3d} site symmetry.[10,30] We found that this is also true for h-LMO. Among three distinct types of Lu ions in a given unit cell of the polar $P6_3cm$ phase, two Lu ions shift downward along the c-axis while the third ion moves upward for the downward polarization [Fig. 1(b)]. As the three local dipoles do not cancel each other, the net ferroelectric polarization develops along the c-axis. On the other hand, the net off-centering distortion in the MnO$_5$ unit having D_{3h} site symmetry is relatively negligible [Fig. 1(b)], indicating this bipyramidal unit is not responsible for the manifestation of ferroelectricity in h-LMO or h-RMnO$_3$, in general.[10,30]

Several conceivable spin structures were considered as the ground-state Mn-spin configuration in the triangular sublattice of h-RMnO$_3$.[31] Accordingly, we have computed the Kohn-Sham (K-S) energy of h-LMO for the four distinct noncollinear spin configurations as schematically depicted in Fig. 2. It is shown that the K-S energy is essentially independent of the spin configuration adopted: 0.00018, 0.00017, 0.00005, and 0.0 eV per formula unit for the spin configurations (a), (b), (c), and (d), respectively. This suggests that h-LMO is nearly characterized by multiply degenerate ground-state spin configurations. In our subsequent calculations, we adopted a noncollinear triangular AFM spin configuration as shown in Fig. 2(d). This triangular spin configuration is largely consistent with a typical spin structure adopted for frustrated triangular AFM spins in hexagonal manganites, h-RMnO$_3$.[9,32] In this case, one would expect a nearly zero residual magnetic moment along the in-plane a-b direction. According to our DFT calculations, however, Mn^{3+} spins are slightly canted with a non-zero moment of 0.004 μ_B (Bohr magneton) per formula unit along the out-of-plane c-direction.

$P6_3/mmc$-$P6_3cm$ phase transition

Let us now consider a possible phase-transition path that would lead to the ferroelectric ground state of $P6_3cm$ symmetry. According to group theoretical analysis,[18,33] we have three conceivable transition paths that connects the high-temperature paraelectric $P6_3/mmc$ phase to the ground-state $P6_3cm$ phase [Fig. 3(a)]. The first allowed path refers to a phase-transition sequence of $P6_3/mmc$-$P6_3mc$-$P6_3cm$ with decreasing temperature. In this path, the transition to the intermediate ferroelectric $P6_3mc$ phase from the prototypic (paraelectric) $P6_3/mmc$ phase is mediated by the freezing-in of the zone-center polar Γ_2^- phonon. On the other hand, the second possible transition path denotes a transition sequence of $P6_3/mmc$-$P6_3/mcm$-$P6_3cm$.[33] In this case, the zone-tripling transition to the intermediate paraeletric phase of $P6_3/mcm$ from the prototypic $P6_3/mmc$ phase is mediated by the freezing-in of the zone-boundary K$_1$ phonon at q = ($1/3,1/3,0$) [Fig. 3(a)]. This first-order transition to the intermediate $P6_3/mcm$ phase is followed by a second-order proper ferroic transition to the polar $P6_3cm$ phase. The third possible path refers to the direct one-step $P6_3/mmc$-$P6_3cm$ zone-tripling transition which involves the freezing-in of the zone-boundary K$_3$ phonon [Fig. 3(a)].[18,33]

To identify the transition path responsible for the appearance of the polar $P6_3cm$ ferroelectric ground state, we have decomposed the atomic displacements that relate the prototypic $P6_3/mmc$ phase to the low-temperature polar $P6_3cm$ phase into the symmetry-adapted modes of the prototypic phase in h-LMO, namely, Γ_2^-, K$_1$, and K$_3$. The computed atomic displacement eigenvectors for the three relevant phonons are schematically shown in Fig. 3(b). The relative strength of each mode in the ferroelectric structure can be quantified by evaluating its amplitude.[34] The calculated mode amplitudes Q_α for all three relevant phonons, Γ_2^-, K$_1$, and K$_3$, are presented in Table I.

The relative sizes of the symmetry-adapted mode amplitudes can be used to judge the path responsible for the transition to

the $P6_3cm$ ferroelectric ground-state structure. According to the computed amplitudes, Q_{K1} is negligibly smaller than Q_{K3} or $Q_{\Gamma_2^-}$ (Table I). Thus, a transition sequence of $P6_3/mmc$-$P6_3/mcm$-$P6_3cm$ (the second path mediated by the nonolar K_1 phonon) can be ruled out. First-principles calculations of the Kohn-Sham energy as a function of the fractional amplitude further distinguish between the first path and the third path. As shown in Fig. 4(a), the prototypic $P6_3/mmc$ phase is stable with respect to the fractional displacement for the polar Γ_2^- mode. This indicates that the transition to the intermediate ferroelectric $P6_3mc$ phase [*i.e.*, the first path in Fig. 3(a)] is highly unlikely to occur. On the contrary, the prototypic $P6_3/mmc$ phase is unstable with respect to the fractional displacement for the K_3 mode (Q_{K3}) and the computed K-S energy exhibits a double-well potential, which demonstrates the relative stability of the ferroelectric $P6_3cm$ phase over the nonpolar $P6_3/mmc$ phase [Fig. 4(b)]. Thus, the manifestation of the $P6_3cm$ hexagonal ferroelectricity in *h*-LMO can be attributed to the direct one-step transition to the $P6_3cm$ ferroelectric ground state from the prototypic nonpolar $P6_3/mmc$ state *via* the third transition path [Fig. 3(a)].

Polarization induced by phonon mode coupling

The third transition path, however, is mediated by the freezing-in of the nonpolar K_3 phonon. On the other hand, the globally polar $P6_3cm$ structure requires a condensation of the polar Γ_2^- phonon. This suggests a coupling of the nonpolar K_3 mode with the polar Γ_2^- mode, producing a non-zero equilibrium value of $Q_{\Gamma_2^-}$. We have then considered the phonon part of the free-energy density ($\mathcal{F}_p$) to quantitatively assess the degree of this mode-mode coupling. Expanding the Landau free-energy invariant to the fourth order in Q_{K3} and $Q_{\Gamma_2^-}$ with the coupling between them, we obtain[33]:

$$\mathcal{F}_p(Q_{K_3}, Q_{\Gamma_2^-}) = \alpha_{20}Q_{K_3}^2 + \alpha_{02}Q_{\Gamma_2^-}^2 + \beta_{40}Q_{K_3}^4 + \beta_{04}Q_{\Gamma_2^-}^4$$
$$+ \gamma_{31}Q_{K_3}^3Q_{\Gamma_2^-} + \gamma_{22}Q_{K_3}^2Q_{\Gamma_2^-}^2 \qquad (1)$$

where the last two terms take care of the symmetry-allowed coupling between these two phonon modes. Identifying the phonon part of the K-S energy (with respect to the centro-symmetric $P6_3/mmc$ state where Q = 0) with $\mathcal{F}_p$, one can obtain optimized expansion coefficients by exploiting the K-S energy calculations. For this, we performed a series of K-S energy calculations as a function of $Q_{\Gamma_2^-}$ under the condition of $Q_{K3} = 0$ (i.e., in the absence of coupling). Similarly, we carried out K-S energy calculations as a function of Q_{K3} under the condition of $Q_{\Gamma_2^-} = 0$. The following four expansion coefficients were then obtained by nonlinear fitting: α_{02} = +0.2089 eV, β_{04} = +0.0116 eV, and α_{20} = -2.7916 eV, β_{40} = +2.0508 eV. The two coupling coefficients were subsequently fit using the computed $Q_{\Gamma_2^-}$-dependent K-S energy for various values of Q_{K3} (Fig. 5): γ_{31} = -0.5367 eV, γ_{22} = +0.6138 eV.

It is interesting to notice that the K-S energy plotted as a function of Q_{K3} does not show its minimum at $Q_{K3} = \pm 1$ [red squares in Fig. 4(b)]. We are now able to explain this apparent anomaly using the optimized coefficients obtained previously.

E_{KS} in Fig. 4(b) with $Q_{\Gamma_2^-} = 0$ can be identified by $\alpha_{20}Q_{K_3}^2 + \beta_{40}Q_{K_3}^4$ from Eq. (1). The two minima in E_{KS} can be obtained by imposing the equilibrium condition, *i.e.*, $(\partial E_{KS}/\partial Q_{K_3})_{Q_{\Gamma_2^-}=0}$ = 0. Thus, the corresponding Q_{K3} values are $(Q_{K_3})_{min}$ = $\pm\sqrt{(-\alpha_{20}/2\beta_{40})}$ = $\pm 0.83 < 1$. This suggests that the $K_3 \leftrightarrow \Gamma_2^-$ mode coupling is needed for a complete transformation to the polar $P6_3cm$ structure from the prototypic $P6_3/mmc$ structure *via* the third transition path.

Having obtained a clue for the $K_3 \leftrightarrow \Gamma_2^-$ mode coupling, we are now able to critically examine the role of this phonon coupling in the manifestation of the ferroelectric polarization. The mode coupling can be realized by plotting E_{KS} as a function of $Q_{\Gamma_2^-}$ for various values of Q_{K3}. It is interesting to notice that the equilibrium position of $Q_{\Gamma_2^-}$ shifts to a positive value and continues to increase with increasing Q_{K3} [Fig. 5]. According to the computed result, the K_3 mode does not destabilize the polar Γ_2^- mode, but pushes $Q_{\Gamma_2^-}$ to a non-zero equilibrium position, playing a role of 'a geometric field'[33] since the coupling-induced polarization can be shown to be proportional to either Q_{K3} or Q_{K3}^3 depending on the magnitude of Q_{K3}. Thus, one can identify the K_3 mode as the primary order parameter and the transverse optical (TO) Γ_2^- mode as a secondary parameter. All these computed results clearly indicate that the ferroelectric polarization ($\mathbf{P_s}$) which is proportional to $Q_{\Gamma_2^-}$ is triggered by the coupling of the nonpolar unstable K_3 mode with the polar Γ_2^- mode.

Having identified the role of the $K_3 \leftrightarrow \Gamma_2^-$ mode coupling in the manifestation of $\mathbf{P_s}$, let us go back to our puzzling question: What is the microscopic origin of the observed large temperature-gap between the structural transition to the polar $P6_3cm$ phase (at ~1290 K) and the emergence of $\mathbf{P_s}$ (at ~750 K)? To elucidate this question, we have divided the Q_{K3}-dependent $\mathbf{P_s}$ into two distinct regions by imposing the equilibrium condition to Eq. (1) with respect to $Q_{\Gamma_2^-}$, *i.e.* $(\partial \mathcal{F}_p/\partial Q_{\Gamma_2^-})_{Q_{K3}}$ = 0. If $Q_{K3} \ll (\alpha_{02}/\gamma_{22})^{1/2}$, the following inequality relation is obviously valid: $\alpha_{02} \gg 2\beta_{04}Q_{\Gamma_2^-}^2$. Under this condition, $\mathbf{P_s}$ remains at a very small value (Region I) and we establish the following expression for $Q_{\Gamma_2^-}$.

$$\text{(Region I)} \quad Q_{\Gamma_2^-} = (-\gamma_{31}/2\alpha_{02})Q_{K3}^3 \qquad (2)$$

On the other hand, if $Q_{K3} \gg (\alpha_{02}/\gamma_{22})^{1/2}$ (Region II), $Q_{\Gamma_2^-}$ is simply proportional to Q_{K3}.

$$\text{(Region II)} \quad Q_{\Gamma_2^-} = (-\gamma_{31}/2\gamma_{22})Q_{K3} \qquad (3)$$

As Q_{K3} is the primary order parameter, we have computed the Q_{K3}-dependent $\mathbf{P_s}$ by exploiting the Berry phase method.[26] For this, we have to evaluate the equilibrium value of $Q_{\Gamma_2^-}$ first by computing the $Q_{\Gamma_2^-}$-dependent K-S energy for each selected value of Q_{K3}. As shown in Fig. 6, $\mathbf{P_s}$ remains at a very small value owing to the $Q_{K_3}^3$–dependence in Region I. For Q_{K3} greater than a certain critical value (Region II), the coupling of the polar Γ_2^- mode with the nonpolar K_3 mode is practically turned on and $\mathbf{P_s}$, thus $Q_{\Gamma_2^-}$, is linearly proportional to Q_{K3}. The existence of Region I having a small $\mathbf{P_s}$ (Fig. 6) explains the

observed large temperature-gap between the structural phase transition at ~1290 K and the para-to-ferroelectric transition at ~750 K. Thus, *h*-LMO undergoes a structural transition to *P6₃cm* polar symmetry below ~1290 K but its $\mathbf{P_s}$ remains at a very small value down to ~750 K (Region I). As the Q_{K3}^3-Q_{K3} crossover occurs at ~750 K, *h*-LMO enters into Region II and its $\mathbf{P_s}$ is practically turned on owing to the $K_3 \leftrightarrow \Gamma_2^-$ mode coupling. This type of mode-coupling arguments can be extended to other hexagonal rare-earth manganites that exhibit a large temperature-gap (ΔT_h) such as *h*-YMnO₃, *h*-ErMnO₃, and *h*-YbMnO₃.[18]

Asymmetric Lu-O bonding and ferroelectricity

We then examined the asymmetric chemical bonding directly related to an off-centering ferroelectric distortion along the *c*-axis. For this purpose, we have compared the computed electron localization function (ELF) of the paraelectric *P6₃/mmc* phase with that of the *P6₃cm* phase as the ELF is known to be an informative tool to distinguish different bonding interactions.[11] As shown in Fig. 7(a), the computed ELF value of the region between the Lu ion and the axial O_A is negligible in the *P6₃/mmc phase*, which demonstrates a dominant ionic bonding character in the Lu-O_A bond. Upon the transition to the ferroelectric *P6₃cm* phase, the Lu ion moves to an asymmetric position and there occurs asymmetric bonding interaction between the Lu ion and one of the two O_A ions along the *c*-axis. This results in a spontaneous breaking of the centrosymmetric state. Contrary to this, there is no noticeable variation in the computed ELF for both Lu-O_I and Mn-O_I bonds.

To clearly visualize the change in the localized electron density associated with the *P6₃/mmc-P6₃cm* phase transition, we also present the difference in the electron localization function ($\delta ELF(\mathbf{r})$) between the ferroelectric and paraelectric states.[30,35] As presented in Fig. 7(b), the $\delta ELF(\mathbf{r})$ contour clearly shows asymmetric movements of Lu and O_A ions and a strong asymmetric electron localization along the *c*-axis upon the transition to the ferroelectric *P6₃cm* state. All these computed results thus suggest that the asymmetric Lu-O_A bonding interaction is directly related to the paraelectric-to-ferroelectric transition in *h*-LMO.

The computed Born effective charge (BEC) tensors interestingly support the asymmetric covalent-bonding interaction between Lu and O_A in the ferroelectric *P6₃cm* phase. As shown in Table II, the BEC tensor of Lu ion for the in-plane (*xx* or *yy*) direction decreases while the BEC tensor for the out-of-plane (*zz*) direction increases markedly upon the transition to the polar *P6₃cm* phase. The same tendency is also obtained for the BEC tensor of O_A (Table II). Thus, the enhanced *zz*-component of the BEC tensor correlates well with the enhanced asymmetric covalent bonding between Lu and O_A along the *c*-axis upon the transition to the ferroelectric *P6₃cm* structure.

Having demonstrated asymmetric Lu-O_A covalent-bonding interaction associated with the transition to the *P6₃cm* state, we now address the following issue: What kind of orbital interaction is involved in the asymmetric Lu³⁺-O_A bonding? To answer this question, we have considered two distinct

possibilities of the Lu³⁺-O_A bonding interaction. As schematically shown in Fig. 8(a), these are (i) empty $5d_z^2$(Lu)-$2p_z(O_A)$ interaction and (ii) empty $6s$(Lu)-$2p_z(O_A)$ interaction. Both types of hybridization induce asymmetric covalent bonding along the *c*-axis of *P6₃cm*. In this way, the central Lu ion is now able to make an asymmetric covalent bond with one of the two neighboring O_A ions (but not simultaneously with two neighboring O_A ions), which results in a spontaneous breaking of the centrosymmetric state.

We have then examined partial density of states (PDOS) for several atomic orbitals relevant to the asymmetric covalent-bonding interaction. As shown in Fig. 8(b), there is little tendency of the orbital hybridization between $6s$(Lu) and $2p_z(O_A)$ for both paraelectric (*P6₃/mmc*) and ferroelectric (*P6₃cm*) states. Contrary to this, there is a strong overlapping of the Lu $5d_z^2$-orbital PDOS with the O_A $2p_z$-orbital PDOS in the valence-bonding energy region (between -1.5 and 0 eV below the valence-band top). This overlapping is remarkably enhanced upon the transition to the polar *P6₃cm* state. Thus, the $5d_z^2$(Lu)-$2p_z(O_A)$ hybridization is primarily responsible for the asymmetric covalent-bonding interaction along the *c*-axis of *P6₃cm*. However, the $5d_z^2$(Lu)-$2p_z(O_A)$ asymmetric covalent bonding cannot be the main driving force of ferroelectricity in *h*-LMO since the prototypic *P6₃/mmc* phase is stable with respect to the fractional displacement for the polar Γ_2^- mode ($Q_{\Gamma_2^-}$) [Fig. 4(a)]. On the contrary, the $5d_z^2$(Lu)-$2p_z(O_A)$ hybridization allows the K_3 mode to be unstable through antipolar distortions along the *c*-axis [Fig. 4(b)]. This pushes $Q_{\Gamma_2^-}$ to a non-zero equilibrium position through the $K_3 \leftrightarrow \Gamma_2^-$ mode coupling [Fig. 5]. Thus, the orbital hybridization plays an indirect role in the manifestation of the hexagonal ferroelectricity in *h*-LMO.

4. Conclusions

In conclusion, the phase transition to the polar *P6₃cm* structure is mediated by the freezing-in of the zone-boundary K_3 phonon. However, the ferroelectric polarization remains at a negligibly small value until Q_{K3} becomes a certain critical value above which the coupling of the polar Γ_2^- mode with the nonpolar K_3 mode is practically turned on. This mode-coupling-induced polarization explains the observed temperature-gap in *h*-LMO as well as other rare-earth manganites.

Acknowledgements

Notes and references

ᵃDivision of Advanced Materials Science (AMS) and Department of Materials Science and Engineering, Pohang University of Science and Technology (POSTECH), Pohang 790-784, Republic of Korea.
ᵇDepartment of Physics, Pohang University of Science and Technology (POSTECH), Pohang 790-784, Republic of Korea.
Corresponding author, E-mail: hmjang@postech.ac.kr; Tel: +82-54-279-2138

1   G. A. Smolenski and I. E. Chupis, *Soviet Physics Uspekhi*, 1982, **25,** 475.

2   J. Wang, J. B. Neaton, H. Zheng, V. Nagarajan, S. B. Ogale, B. Liu, D. Viehland, V. Vaithyanathan, D. G. Schlom, U. V. Waghmare, N. A. Spaldin, K. M. Rabe, M. Wuttig, and R. Ramesh, *Science*, 2003, **299,** 1719.

3   T. Kimura, T. Goto, H. Shintani, K. Ishizaka, T. Arima, and Y. Tokura, *Nature*, 2003, **426,** 55.

4   N. Hur, S. Park, P. A. Sharma, J. S. Ahn, S. Guha, and S. W. Cheong, *Nature*, 2004, **429,** 392.

5   T. Lottermoser, T. Lonkai, U. Amann, D. Hohlwein, J. Ihringer, and M. Fiebig, *Nature*, 2004, **430,** 541.

6   W. Eerenstein, N. D. Mathur, and J. F. Scott, *Nature*, 2006, **442,** 759.

7   S.-W. Cheong and M. Mostovoy, *Nat Mater*, 2007, **6,** 13.

8   P. Tolédano, W. Schranz, and G. Krexner, *Phys. Rev. B*, 2009, **79,** 144103.

9   C.-Y. Ren, *Phys. Rev. B*, 2009, **79,** 125113.

10 B. B. Van Aken, T. T. M. Palstra, A. Filippetti, and N. A. Spaldin, *Nat. Mater*, 2004, **3,** 164.

11 M.-A. Oak, J.-H. Lee, H. M. Jang, J. S. Goh, H. J. Choi, and J. F. Scott, *Phys. Rev. Lett.*, 2011, **106,** 047601.

12 H. L. Yakel, W. C. Koehler, E. F. Bertaud, and E. F. Forrat, *Acta Crystallogr.*, 1963, **16**, 957.

13 A. A. Bossak, C. Dubourdieu, J.-P. Sénateur, O. Y. Gorbenko, and A. R. Kaul, *J. Mater. Chem.*, 2002, **12**, 800.

14 S. C. Abrahams, *Acta Cryst B*, 2001, **57**, 485.

15 A. S. Gibbs *et al.*, *Phys. Rev. B*, 2005, **83**, 094111.

16 A. Ghosh, J. R. Sahu, S. V. Bhat, and C. N. R. Rao, *Solid. State Sci.*, 2009, **11**, 1639.

17 S.-J. Ahn, J. Kim, N. Shin, and Y.-M. Koo, *J. Appl. Phys.*, 2011, **110**, 084112.

18 T. Lonkai, D. G. Tomuta, U. Amann, J. Ihringer, R. W. A. Hendrikx, D. M. Tbbens, and J. A. Mydosh, *Phys. Rev. B*, 2004, **69**, 134108.

19 J. P. Perdew, K. Burke, and Y. Wang, *Phys. Rev. B*, 1996, **54,** 16533.

20 I. A. Vladimir, F. Aryasetiawan, and A. I. Lichtenstein, *J. Phys.: Condens. Matter*, 1997, **9,** 767.

21 P. E. Blchl, *Phys. Rev. B,* 1994, **50,** 17953; G. Kresse and D. Joubert, *Phys. Rev. B*, 1999, **59,** 1758.

22 G. Kresse and J. Furthmüller, *Phys. Rev. B*, 1996, **54,** 11169.

23 H. J. Monkhorst and J. D. Pack, *Phys. Rev. B*, 1976, **13,** 5188.

24 P. E. Blchl, O. Jepsen, and O. K. Andersen, *Phys. Rev. B*, 1994, **49,** 16223.

25 J. E. Medvedeva, V. I. Anisimov, M. A. Korotin, O. N. Mryasov, and A. J. Freeman, *J. Phys.: Condens. Matter* 2000, **12**, 4947.

26 R. D. King-Smith and D. Vanderbilt, *Phys. Rev. B*, 1993, **47,** 1651; D. Vanderbilt and R. D. King-Smith, *Phys. Rev. B*, 1993, **48,** 4442.

27 M. I. Aroyo, A. Kirov, C. Capillas, J. M. Perez-Mato, and H. Wondratschek, *Acta Cryst. A*, **62**, 115 (2006); M. I. Aroyo, J. M. Perez-Mato, C. Capillas, E. Kroumova, S. Ivantchev, G. Madariaga, A. Kirov, and H. Wondratschek, *Zeit. Krist.*, 2006, **221,** 15.

28 D. Orobengoa, C. Capillas, M. I. Aroyo, and J. M. Perez-Mato, *J. Appl. Cryst.*, 2009, **42**, 820; J. M. Perez-Mato, D. Orobengoa, and M. I. Aroyo, *Acta Cryst.*, 2010, **66**, 558.

29 M. C. Payne, M. P. Teter, D. C. Allan, T. A. Arias, and J. D. Joannopoulos, *Rev. of Mod. Phys.*, 1992, **64,** 1045.

30 M.-A. Oak, J.-H. Lee, and H. M. Jang, *Phys. Rev. B*, 2011, **84,** 153106.

31 C. C. Zhong, X. F. Jiang, H. L. Yu, Q. Jiang, J. H. Fang, and Z. Y. Li, *J. Mag. & Mag. Mater.*, 2009, **321,** 1260.

32 T. Katsufuji, M. Masaki, A. Machida, M. Moritomo, K. Kato, E. Nishibori, M. Takata, M. Sakata, K. Ohoyama, K. Kitazawa, and H. Takagi, *Phys. Rev. B*, 2002, **66**, 134434.

33 C. Fennie and K. M. Rabe, *Phys. Rev. B*, 2005, **72,** 100103.

34 T. Hashimoto, T. Nishimatsu, H. Mizuseki, Y. Kawazoe, A. Sasaki, and Y. Ikeda, *Jpn. J. Appl. Phys.*, 2004, **43** [9B], 6785.

35 A, Stroppa, M. Marsman, G. Kresse, and S. Picozzi, *New J. Phys.*, 2010, **12**, 093026.

TABLE I. Decomposition of the atomic displacements (Å) into the symmetry-adapted modes of the prototypic $P6_3/mmc$ phase in h-LMO. The mode amplitudes, Q, are shown in Å.

	Γ_2^-	K_1	K_3	
	[001]	[100]	[100]	[001]
Lu1	-0.0514	0	0	0.3333
Lu2	-0.0514	0	0	-0.1667
Mn	-0.0457	-0.0008	0	0
$O_{ap}(1)$	0.0089	0.0005	-0.1709	0
$O_{ap}(2)$	0.0089	0.0005	0.1709	0
$O_{eq}(3)$	0.0882	0	0	-0.4226
$O_{eq}(4)$	0.0882	0	0	0.2112
Q_{calc}	**0.276**	**0.003**	**1.104**	

TABLE II. The computed Born effective charge tensors ($Z^*_{\kappa,\alpha\beta}$; scalar) of Lu and O_A for the paraelectric $P6_3/mmc$ and ferroelectric $P6_3cm$ phases of h-LMO. The Born effective charge is defined by $Z^*_{\kappa,\alpha\beta} = [\Omega(\partial P_\alpha/\partial\mu_{\kappa,\beta})|_{E=0}]/e$, where Ω is the unit-cell volume [m^3], P is the total field-induced polarization [C/m^2], μ_κ is the displacement of the κth atom [m], and e is the elementary charge [C].

Structure	Ion	Position	Axis		
			xx	yy	zz
$P6_3/mmc$	Lu	2a(0,0,z)	4.28	3.87	3.92
	O_A	2a(0,0,z)	-3.21	-3.71	-1.60
$P6_3cm$	Lu	2a(0,0,z)	3.98	3.79	4.66
	O_A	2a(0,0,z)	-3.13	-3.04	-1.81

* Figure Captions

FIG. 1 (Color online). Crystal and off-centering structures of h-LuMnO$_3$ (h-LMO). **(a)** The crystal structure of the paraelectric $P6_3/mmc$ phase is compared with that of the ferroelectric $P6_3cm$ phase. **(b)** The three distinct LuO$_8$ units and the MnO$_5$ bipyramidal unit in the ferroelectric state. Asymmetry in the computed bond distance between Lu and O$_A$ indicates a non-zero off-centering displacement in the LuO$_8$ unit along the c-axis. The three green-colored arrows indicate the direction of the off-centering displacement in each LuO$_8$ unit.

FIG. 2 (Color online). A schematic representation of the four distinct noncollinear spin configurations used in our calculations of the spin-structure-dependent Kohn-Sham energy. Here the arrows at the blue-colored Mn ions denote the directions of the Mn-magnetic moments on the a-b plane at $z = 0$ while the arrows at the green-colored Mn ions represent the directions on the a-b plane at $z = 1/2$.

FIG. 3 (Color online). **(a)** Group theoretically allowed three possible phase transition paths from prototypic $P6_3/mmc$ to ferroelectric $P6_3cm$. **(b)** The computed atomic displacement eigenvectors (denoted by green arrows) schematically represented for the three relevant phonons, Γ_2^-, K_1 and K_3.

FIG. 4 (Color online). **(a)** The Kohn-Sham energy plotted as a function of the fractional amplitude $Q_{\Gamma_2^-}$ under the condition of $Q_{K_3} = 0$. The reference state of $Q_{\Gamma_2^-}=0$ denotes the prototypic $P6_3/mmc$ phase. Herein, $Q_{\Gamma_2^-} = 1$ corresponds to 0.276 Å. The computed atomic displacement eigenvectors in the ferroelectrically active LuO$_8$ unit are displayed in the right-hand side (blue arrows) for the polar Γ_2^- mode. **(b)** The Kohn-Sham energy plotted as a function of Q_{K_3} under the condition of $Q_{\Gamma_2^-} = 0$. Herein, $Q_{K_3} = 1$ corresponds to 1.104 Å. The computed atomic displacement eigenvectors in the two distinct LuO$_8$ units, Lu1 (= Lu2) and Lu3, are displayed in the right-hand side (blue arrows) for the nonpolar K$_3$ mode.

FIG. 5 (Color online). The Kohn-Sham energy plotted as a function of $Q_{\Gamma_2^-}$ for various values of Q_{K3}. The computed result shows that the K$_3$ mode pushes $Q_{\Gamma_2^-}$ to a non-zero equilibrium position, playing a role of 'a geometric field.'

FIG. 6 (Color online). The computed $Q_{\Gamma_2^-}$ and polarization plotted as a function of Q_{K3}.

FIG. 7 (Color online). **(a)** A comparison of the three-dimensional ELF contour of the paraelectric $P6_3/mmc$ phase (left) with that of the ferroelectric $P6_3cm$ phase (right). A left-hand-side bar represents the electron-isosurface gradation adopted in the ELF contour with the isosurface level of 0.06e/Å^3. Red arrows appeared in the $P6_3cm$ phase denote the direction of the off-centering displacement from the centrosymmetric position upon the transition to the polar $P6_3cm$ phase. **(b)** The difference in the computed ELF between the ferroelectric $P6_3cm$ phase and the paraelectric $P6_3/mmc$ phase in h-LMO. The δELF(r) contour on (110)$_h$ is presented in the figure.

FIG. 8 (Color online). **(a)** Schematic diagrams of the two distinct possibilities of the Lu^{3+}-O$_A$ bonding interaction in h-LMO: (i) $5d_z^2$(Lu)-$2p_z$(O$_A$) orbital interaction and (ii) $6s$(Lu)-$2p_z$(O$_A$) orbital interaction. **(b)** A comparison of the orbital-resolved partial density of states for $5d_z^2$(Lu), $6s$(Lu), $2p_x$ or $2p_y$(O$_A$) and $2p_z$(O$_A$) orbitals of the paraelectric $P6_3/mmc$ phase with those of the ferroelectric $P6_3cm$ phase.
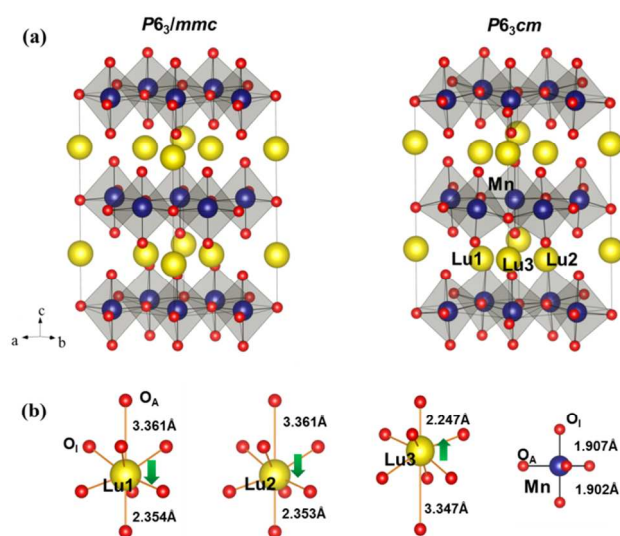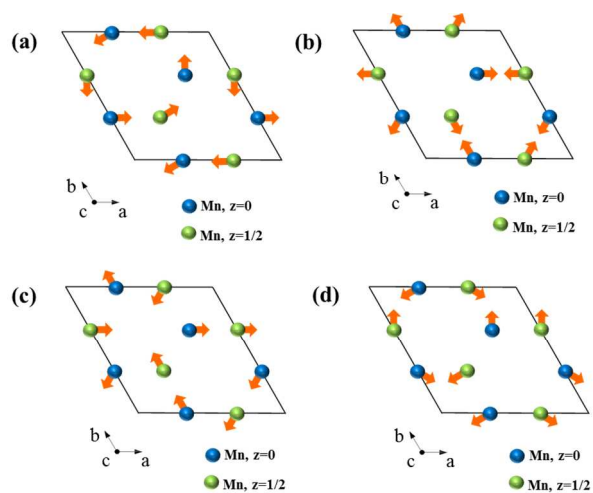
FIG. 1

FIG. 2

FIG. 3

FIG. 4

FIG. 5

FIG. 6

FIG. 7

FIG. 8